nature astronomy

LETTERS

https://doi.org/10.1038/s41550-018-0414-3

Galactic bulge preferred over dark matter for the Galactic centre gamma-ray excess

Oscar Macias[1]*, Chris Gordon[2], Roland M. Crocker[3], Brendan Coleman[2], Dylan Paterson[2], Shunsaku Horiuchi[1] and Martin Pohl[4,5]

An anomalous gamma-ray excess emission has been found in the Fermi Large Area Telescope data[1] covering the centre of the Galaxy[2,3]. Several theories have been proposed for this 'Galactic centre excess'. They include self-annihilation of dark-matter particles[4], an unresolved population of millisecond pulsars[5], an unresolved population of young pulsars[6], or a series of burst events[7]. Here, we report on an analysis that exploits hydrodynamical modelling to register the position of interstellar gas associated with diffuse Galactic gamma-ray emission. We find evidence that the Galactic centre excess gamma rays are statistically better described by the stellar over-density in the Galactic bulge and the nuclear stellar bulge, rather than a spherical excess. Given its non-spherical nature, we argue that the Galactic centre excess is not a dark-matter phenomenon but rather associated with the stellar population of the Galactic bulge and the nuclear bulge.

The main challenge in pinning down the properties of the Galactic centre excess (GCE) is the modelling of diffuse Galactic emission from the interaction of cosmic rays with interstellar gas and radiation fields, by far the dominant source of gamma rays in this region. The Fermi-Large Area Telescope (LAT) Collaboration designed a diffuse Galactic emission model based on a template[8] approach that is optimized to single out gamma-ray point sources. This approach presupposes that the diffuse Galactic emission can be modelled as a linear combination of interstellar gas, inverse Compton maps, and several other diffuse components. Owing to the limited kinematic resolution of gas tracers towards the Galactic centre (GC), interstellar gas correlated gamma rays from the GC direction are difficult to disentangle. Previous studies[3,4,9] utilized interstellar gas maps that were constructed with an interpolation approach that assumed circular motion of interstellar gas. This kinematic assumption provides for an estimate of the distance to a part of the interstellar gas. However, it is well established that the Galaxy contains a central bar that causes non-circular motion of interstellar gas in its inner regions, so assuming circularity introduces a significant and avoidable bias to gamma-ray analyses of the GC region[10].

We use Fermi-LAT data accumulated between 4 August 2008 and 4 September 2015 in the 15°×15° region around the GC. Hydrodynamical simulations[10] that account for the effects of the Galactic bar were used to better determine the diffuse Galactic gamma-ray emission. To evaluate the impact that the choice of interstellar gas models has on our results, we also constructed atomic and molecular hydrogen gas maps using an interpolation approach that reproduced those used in most previous gamma-ray analyses of the GC. We split each into four concentric rings, each with its own normalization parameter. Details of the model components and approach are provided in the Methods.

Interstellar gas map templates constructed using the results of hydrodynamical simulations were found to be a better description of the diffuse gamma-ray data than the standard interpolation-based maps with a log likelihood ratio ≈1,362. As we have additional data compared with that used to construct the Fermi-LAT 3FGL catalogue[11] and since we also use a different Galactic diffuse emission model, we searched for new point sources. We found 64 candidates (each with significance $\geq 4\sigma$) in our region of interest that are shown as green crosses in Fig. 1. We found multi-wavelength counterparts for 18 of our 64 point source candidates. This is similar to the 3FGL catalogue[11] where ~1/3 of the point sources do not have multi-wavelength associations, especially in the GC region where there is high extinction and the diffuse Galactic emission model is more likely to require corrections. Given that our point source candidates have high statistical significance, including them quantitatively affects our results; however, they do not qualitatively affect our conclusions (see section 'Systematic errors' in the Methods).

Our dark-matter template for the GCE is modelled by the square of an Navarro–Frenk–White (NFW) template with an inner slope of 1.2. Note that when all the uncertainties are accounted for, observations of the dwarf spheroidals do not definitively rule out the dark-matter interpretation of the GCE[12]. Extended gamma-ray emission in the GC may also arise from unresolved sources such as millisecond pulsars (MSPs)[5,9] or young pulsars[6], both of which have GeV-peaked gamma-ray spectra. Studies have also shown detectable non-Poissonian features in photon statistics[13,14]. However, these may be due to defects in the Galactic emission model[15]. The young pulsar hypothesis requires recent star formation given the few-Myr gamma-ray lifetimes of ordinary pulsars. Such star formation is absent from most of the bulge except in the $r \lesssim 100\,\mathrm{pc}$ nuclear region; a young pulsar explanation of the GCE thus requires that the bulge contain pulsars that are launched out of the nucleus. It has been claimed that this can be achieved by the pulsar's natal kicks[6] whereas MSPs can be generated from old stellar populations[16].

We thus also consider Galactic bulge stellar templates. Almost half of the stars[17] in the Galactic bulge are on orbits that contribute to the appearance (from the Earth) of an X-shaped over-concentration (the 'X-bulge')[18]. This structure has been revealed in an analysis[19] of 3.4 and 4.6 μm data collected by the WISE telescope[20]. However, in ref. [21], it is argued that the X-shape is a processing artefact. Our aim is not to scrutinize what the correct bulge template may be, but rather to explore the bulge as an example astrophysical template for the GCE that is an alternative to dark matter. Using

---

[1]Center for Neutrino Physics, Department of Physics, Virginia Tech, Blacksburg, VA, USA. [2]School of Physical and Chemical Sciences, University of Canterbury, Christchurch, New Zealand. [3]Research School of Astronomy and Astrophysics, Australian National University, Canberra, Australia. [4]Institute of Physics and Astronomy, University of Potsdam, Potsdam-Golm, Germany. [5]DESY, Zeuthen, Germany. *e-mail: oscar.macias@vt.edu

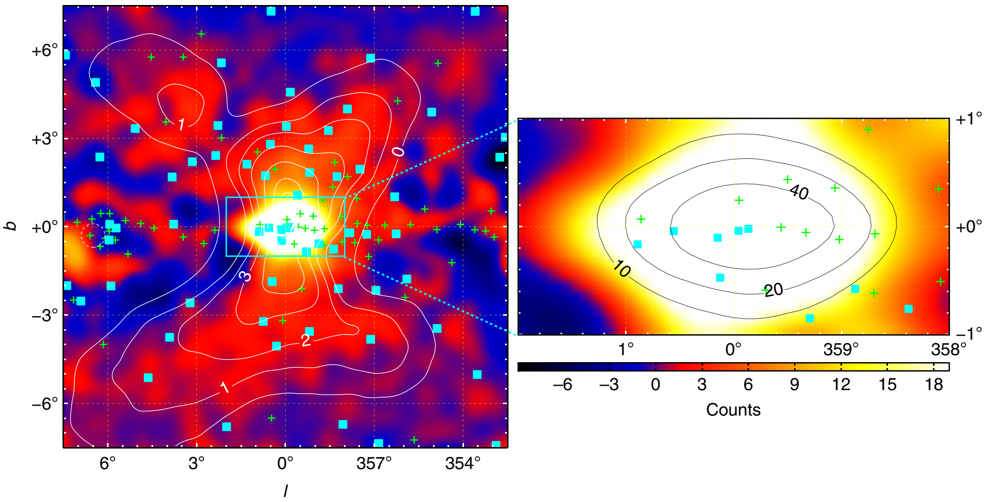

Fig. 1 | Residual map of the 15° × 15° region of interest for $E \geq 667$ MeV. The residuals are obtained as data − model, where the model includes previously detected 3FGL point sources (cyan squares)[11], 64 additional point source candidates (green crosses) and the standard diffuse Galactic emission components related to the interstellar gas and radiation field. The white contours are the best-fit model counts from the X-bulge map obtained from analyses of WISE[19] infrared data after convolution of the Fermi-LAT instrument response function. The addition of a template based on the X-bulge significantly improved the model fit to the gamma-ray data. The cluster of point sources on the Galactic plane at $l \approx 6°$ may be associated with the W28 (white dashed circle) supernova remnant[11,31]. The zoomed-in region on the right shows the correlation with the near-infrared stellar density nuclear bulge data[23]; the black contours display the best-fit model counts associated with this component after convolution with the Fermi-LAT instrument response function. The X-bulge and nuclear bulge templates were included when the best-fit parameters for the above model were found, but not when evaluating the above residuals. A Gaussian with radius 0.3° was used to smooth the images and the upper limit of the colour scale has also been clipped for display purposes.

Table 1 | Summary of the likelihood analysis results

Base	Source	log($\mathscr{L}_{\text{Base}}$)	log($\mathscr{L}_{\text{Base+Source}}$)	TS$_{\text{Source}}$	σ	Number of source parameters
Baseline	FB	−172,461.4	−172,422.3	78	6.9	19
Baseline	NFW-s	−172,461.4	−172,265.3	392	18.4	19
Baseline	Boxy bulge	−172,461.4	−172,238.7	445	19.7	19
Baseline	X-bulge	−172,461.4	−172,224.1	475	20.5	19
Baseline	NFW	−172,461.4	−172,167.9	587	23.0	19
Baseline	NB	−172,461.4	−171,991.8	939	29.5	19
Baseline	NP	−172,461.4	−169,804.1	5315	55.7	64 × 19
Baseline+NP	FB	−169,804.1	−169,773.6	61	5.8	19
Baseline+NP	NB	−169,804.1	−169,697.2	214	13.0	19
Baseline+NP	Boxy bulge	−169,804.1	−169,663.7	281	15.3	19
Baseline+NP	NFW	−169,804.1	−169,623.3	362	17.6	19
Baseline+NP	X-bulge	−169,804.1	−169,616.2	376	18.0	19
Baseline+NP+X-bulge	NFW	−169,616.2	−169,568.4	96	7.9	19
Baseline+NP+X-bulge	NB	−169,616.2	−169,542.0	148	10.4	19
Baseline+NP+X-bulge+NB	NFW	−169,542.0	−169,531.0	22	2.4	19
Baseline+NP+X-bulge+NB	FB	−169,542.0	−169,525.5	33	3.5	19
Baseline+NP+NB	X-bulge	−169,697.2	−169,542.0	310	16.1	19
Baseline+NP+NB	Boxy bulge	−169,697.2	−169,566.0	262	14.6	19
Baseline+NP+NFW	X-bulge+NB	−169,623.3	−169,531.0	185	10.8	2 × 19
Baseline+NP+NFW+NB	X-bulge	−169,598.9	−169,531.0	136	9.9	19
Baseline+NP+boxy bulge+NB	NFW	−169,566.0	−169,553.3	25	2.7	19

The baseline model consists of all 3FGL point sources in the region of interest, Loop I, an inverse Compton (IC) template predicted by GALPROP, the hydrodynamic-based gas maps, the recommended isotropic emission map, and a model for the Sun and the Moon. Other model templates considered are: the 64 new point sources (NP), the square of a generalized NFW profile with an inner slope $\gamma = 1.2$ or the square of a 'standard NFW' (NFW-s) with inner slope $\gamma = 1$, an infrared X-bulge and a boxy bulge template tracing old stars in the Galactic bulge, a nuclear bulge (NB) template and a template accounting for the Fermi bubbles (FB). The maximized likelihoods ($\mathscr{L}$) are given for the base and base+source models and the significance of the new source is given by $\text{TS}_{\text{Source}} \equiv 2\,(\log(\mathscr{L}_{\text{Base+Source}}) - \log(\mathscr{L}_{\text{Base}}))$. Note that for both likelihoods, all parameters are maximized and so the $\mathscr{L}_{\text{Base+Source}}$ will have additional parameters whose number is given in the last column. The conversion between TS$_{\text{Source}}$ and σ is discussed in the Methods.

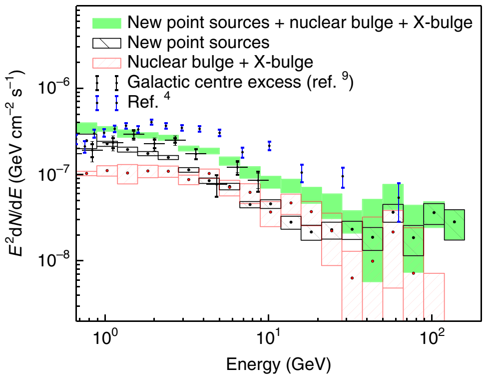

Fig. 2 | Differential flux of the new, statistically significant components in the Galactic centre. The black boxes are the combined spectrum of the 64 new point source candidates, red boxes are the superposition of the nuclear bulge and X-bulge differential fluxes, and the green boxes display the sum of these three components and are compatible with previous results[4,9], although the comparison should only be taken as qualitative as the previous results are for slightly different regions of interest. The box size encompasses the 68% confidence intervals. We found that the combined nuclear bulge and X-bulge spectrum is better fitted by an exponential cut-off rather than a power-law model at 5σ.

standard maximum-likelihood estimation with an X-bulge template based on the average of the 3.4 and 4.6 μm data, we find that the addition of our X-bulge template improves the fit to the gamma-ray data at about the 16.1σ level (Table 1). Note that we do not claim that the X-bulge provides a fit 16.1σ better than any other possible bulge stellar template. What we have done is evaluate how much the likelihood improved when an X-bulge was added relative to the likelihood without any new component being added to account for the GCE. We also tried a boxy-shaped bulge (see Methods), and found that it improves the fit to the data at the 14.6σ level. Importantly, the last row of Table 1 shows that even when the boxy bulge stellar map is considered instead of the X-bulge, the dark-matter template is still confidently ruled out as an explanation of GCE. As the X-bulge has a slightly higher σ than the boxy bulge, we have used the X-bulge in the rest of the paper. Similar results would be obtained with the boxy bulge template.

A further stellar component within the wider Galactic bulge is the so-called nuclear bulge. This disky distribution of stars concentrated within an ~230 pc radius of the Galactic nucleus has experienced on-going star formation over the life of the Galaxy and represents ~10% of the overall bulge mass[22]. To determine whether the nuclear bulge template improves the fit to the Fermi-LAT gamma-ray data, we used a map constructed from a near-infrared stellar density measurement[23] and found a 10σ improvement in the fit (Table 1). In Fig. 1, we show the residual gamma-ray map obtained after subtraction of our best-fit galactic diffuse emission and point sources model. As can be seen, the X-bulge and nuclear bulge are well traced by our residual gamma-ray maps. The correlation with the X-bulge is more evident away from the plane where the hard-to-model diffuse Galactic emission is no longer so dominant and the Poisson noise is much lower. We performed a ±1° masking of the plane and found consistent results (see Methods).

Best-fit spectral parameters were found using χ^2 fitting to the inferred flux points for the energy bins. Relative to a power-law spectrum, the preferred spectral model, at 3.5σ and 5.1σ, respectively, for both the X-bulge and nuclear bulge templates was a power law with an exponential cut-off ($dN/dE \propto E^{-\Gamma}\exp(-E/E_{\mathrm{cut}})$, where N is the photon flux). The X-bulge had a spectral slope of $\Gamma = 1.9 \pm 0.1$, an energy cut-off $E_{\mathrm{cut}} = 10 \pm 5$ GeV and a luminosity $L = (4.5 \pm 0.3) \times 10^{36}$ erg s^{-1} for $E \geq 100$ MeV. Similarly, the fit for the nuclear bulge yielded $\Gamma = 1.9 \pm 0.1$, $E_{\mathrm{cut}} = 13 \pm 4$ GeV and $L = (3.3 \pm 0.3) \times 10^{36}$ erg s^{-1}. Here and throughout the article, 68% confidence intervals are used for error bars and we adopted 8.25 kpc for the distance to the GC. When the X-bulge and nuclear bulge spectra were combined (Fig. 2), we found that a power-law exponential model was still preferred relative to a power-law ($dN/dE \propto E^{-\alpha}$) model at 5.0$\sigma$, where α is the spectral slope. The best-fit spectral parameters for this case are shown in Table 2. The combined X-bulge and nuclear bulge spectral parameters are compatible with previous estimates of the GCE based on templates of dark matter as well as resolved MSPs and globular clusters containing MSPs[9].

When the X-bulge and nuclear bulge templates are included in the fit, we found that a squared NFW template with an inner slope of 1.2 was not significantly detected (Table 1). The 95% upper limit on this component's luminosity was found to be 5×10^{36} erg s^{-1}. The luminosity for an NFW-squared profile from our model baseline+NP+NFW, displayed in Table 2, is consistent with previous estimates[9] and is about an order of magnitude larger than the limit we obtain when the X-bulge and nuclear bulge templates are included. Similarly, a dark-matter template based on the square of an NFW profile with an inner slope of 1.0 was undetected.

The Fermi bubbles[24,25] are lobes that extend up to ~7 kpc from the Galactic plane. The boundaries of the Fermi bubbles are described by two catenary curves[8] (Methods). However, the catenary geometry does not match the excess we see in our residual and test statistic (TS) maps in Fig. 1 and Supplementary Fig. 1. We found that the addition of a catenary template did not qualitatively affect our results. As this template had a low TS value (Table 1) we did not include it in our final results but rather treated its potential presence as a systematic effect (Table 2, Methods and Supplementary Section 3).

A comparison between the properties of our proposed X-bulge and nuclear bulge MSPs with other MSP populations can be obtained by comparing the MSP luminosity to stellar mass ratio. Note that this comparison assumes that the ratio of MSP mass to stellar mass is constant across the different regions considered, which can only be approximately correct. The stellar mass[26] of the Galactic bulge is 1.5×10^{10} solar masses ($M_{\odot}$) and the nuclear bulge has a mass of ~1.4×10^9 $M_{\odot}$. According to ref. [17], instantaneous stellar mass contributing to the appearance of the X-bulge over-density represents about 25% of the Galactic bulge. However, as can be seen by comparing our white contours in Fig. 1 to those

Table 2 | Exponential cut-off best-fit parameters with statistical and systematic errors to the X-bulge+nuclear bulge

Parameter	Best fit	Statistical error	Systematic error				
			Spin temperature	Inverse Compton	Dust	Fermi bubbles	Total
Γ	2.0	0.1	0.1	0.1	0	0.1	0.2
^{E}cut (GeV)	13	5	1	3	1	2	4
$\mathscr{L}$ (10^{36} erg s^{-1})	6	1	1	1	0	0	1

The statistical errors are 1σ. The total systematic error was obtained by adding in quadrature the individual systematic errors. Luminosities were computed for $E > 100$ MeV.

in figure 18 of ref. [17], the method used in ref. [17] to determine this contribution underestimates the X-bulge we extract from the WISE data as it eliminates the central regions of the X-bulge that we have included in our template. Therefore, we estimate our X-bulge has an instantaneous stellar mass $\gtrsim 4\times10^9\ M_\odot$. From these data we infer an $E \geq 100$ MeV luminosity-to-mass (LtM) ratio of $\lesssim 2\times10^{27}$ erg s^{-1} $M_\odot{}^{-1}$ for the combined X-bulge and nuclear bulge structure. This is similar to the LtM ratio we infer from ref. [27] for the MSP emission from the entire Milky Way of ~2×10^{27} erg s^{-1} $M_\odot{}^{-1}$ and less than the ~5×10^{28} erg s$^{-1}M_\odot{}^{-1}$ for globular cluster 47 Tuc[28] (which has an MSP-dominated >100 MeV luminosity of $(4.8\pm1.1)\times10^{34}$ erg s^{-1} and stellar mass of about $10^6\ M_\odot$).

We have shown that the X-bulge (or boxy bulge) plus the nuclear bulge provide a better fit than the dark-matter explanation. We have not explicitly checked the burst model, but current implementations are highly model dependent and fine-tuned[7]. Also, the young pulsar explanation is typically associated with spherically symmetric templates[6] and thus is also disfavoured compared with our MSP-based X-bulge (or boxy bulge)+nuclear bulge explanation. Therefore, we have shown, in agreement with other recent results[29], that the Galactic bulge stellar distribution is preferred over a spherically symmetric NFW-squared excess template.

Methods

Observations. We examined ~7 years of Fermi-LAT data[1] (4 August 2008–4 September 2015) selecting Pass 8 ULTRACLEANVETO class events. The data were extracted from a square region of 15°×15° centred at Galactic coordinates $(l, b) = (0, 0)$ and made no distinction between front and back events. Furthermore, we restricted our analysis to the 667 MeV to 158 GeV energy range and used the P8R2_ULTRACLEANVETO_V6 instrument response functions. To avoid contamination from terrestrial gamma-rays, we used events with zenith angles smaller than 90°. This work made use of the Fermi Science Tools v10r0p5 software package.

Employing the gtmktime tool we selected the recommended data filters (DATA_QUAL>0)&&(LAT_CONFIG==1). Spatial binning was performed with the gtbin utility with which we divided the LAT data into 150×150 angular bins of size 0.1° in a CAR sky projection.

Templates. The Galactic diffuse gamma-rays resulting from the interaction of cosmic-ray electrons and protons with the interstellar gas and radiation field were modelled with a similar method used for the standard Galactic diffuse emission model[8]. We fitted a linear combination of atomic and molecular hydrogen gas templates (Supplementary Figs. 2 and 3), an IC energy-dependent spatial template as obtained with GALPROP[30], specialized templates for the Sun and the Moon, an isotropic component (iso_P8R2_ULTRACLEANVETO_V6_v06.txt), and a model for the gamma-ray emission associated with Loop I (Supplementary Fig. 4).

The atomic and molecular hydrogen gas column densities were each distributed within four Galactocentric annuli to account for the non-uniform cosmic-ray flux in the Galaxy. The construction of these templates is described in Supplementary Section 1.

Bin-by-bin analysis. Similar to other works[3,31], we employed a bin-by-bin analysis technique, in which we split the Fermi-LAT data into 19 logarithmically spaced energy bins. Within each energy bin, we performed a separate maximum-likelihood fit[11] with the pyLikelihood analysis tool. The bin size was chosen to be larger than the LAT energy resolution, but narrow enough that the Galactic emission spectral components can be simply approximated by a power-law model. We note that this bin-by-bin method enables us to evaluate the likelihood for a test source with an arbitrary spectral model and significantly reduces the CPU power required to reach convergence as only the flux normalization of the sources are free to vary during the fits.

Once the bin-by-bin method had converged, the inferred spectrum of each source was either fitted by a power-law or an exponential cut-off model. We denote the photon flux in energy bin i by F_i and its uncertainty by ΔF_i. When energy bins had $\mathrm{TS} < 1$ or $\Delta F_i/F_i > 1$, they were combined with adjacent energy bins until $\mathrm{TS} > 1$ and $\Delta F_i/F_i < 1$.

The errors from the bin-by-bin fit were added in quadrature to the errors caused by the uncertainties in the effective area[11]. These effective area errors were taken to be f_i^{rel} times the predicted flux for bin i. Where f_i^{rel} is interpolated from the values given in ref. [11]. The spectrum was modelled by an exponential cut-off if

$$\mathrm{TS}_{\mathrm{curvature}} \equiv 2(\log\ \mathcal{L}(\mathrm{exp.cutoff}) - \log\ \mathcal{L}(\mathrm{powerlaw})) \geq 9 \tag{1}$$

where $\mathcal{L}(i)$ is the maximum likelihood value for model i.

Comparing hydrodynamic and interpolated gas templates. Initially, we fit the LAT data with a model comprised of the 3FGL[11] point sources present in our region of interest plus four other spatially extended sources (HESS J1825-137, RX J1713.7-3946, W28 and W30) reported in the 3FGL[11]. The spatial templates used to model these extended sources correspond to Version 14.

To identify the most suitable gas templates for our study, we performed a scan in which we evaluated the improvement of the likelihood fit to the region of interest when the gas maps used were the ones created with the interpolation method or the hydrodynamical method (see Supplementary Section 1 for details of their construction). Supplementary Figure 5 shows that the data preferred the hydrodynamical method.

During optimization, the flux normalization of the 3FGL sources were left free in each energy bin. We also simultaneously fitted the 13 diffuse components' (H I annuli, CO annuli, dust templates, Loop I, inverse Compton, and isotropic) normalization but kept the Sun and the Moon fluxes fixed to their nominal values.

Point source search. To check whether any additional point sources are required, we followed a methodology similar to that described in refs [11,32]. We started from our baseline model, which consists of all 3FGL point sources in the region of interest, Loop I, an inverse Compton template predicted by GALPROP, the hydrodynamical-based gas maps, the recommended isotropic emission map, and a model for the Sun and the Moon (Supplementary Section 1). We examined the significance of a trial point source with a power-law spectrum, with a fixed slope of two, at the centre of each pixel. The outcome of this was a residual TS map where the gttsmap utility was used for this step. In accordance with our bin-by-bin method, a residual TS map was computed for each energy bin and these were then added to get a total residual map for the full energy range.

From the total residual TS map, we generated a list of all the pixel clusters with TS values above the detection threshold that looked reasonably isolated under visual inspection (~0.5° of angular separation). The coordinates of the source candidates were calculated as the average of adjacent pixel positions weighted by their respective TS values[32]. A more sophisticated technique would be to fit the TS map with a two-dimensional parabola. But we found our results were not sensitive to the small difference in position that this gave. To avoid convergence issues, at each step we added only the ten (or fewer if less were available) brightest seeds to our model and re-ran the bin-by-bin analysis routine where all components—including the new point sources—were simultaneously fitted. Only the seeds that were found to have a TS above the detection threshold from this step were allowed to stay in the model. Note that this is an iterative procedure that goes from bright sources to faint ones. This procedure was repeated seven times in our region of interest until no seeds were found or no more point source candidates passed the thresholding step. This made the method more robust against source confusion. When doing a global analysis, as opposed to a bin-by-bin analysis, each new point source candidate has two parameters for the power law and two parameters for its position. In that case, a $\mathrm{TS} \geq 25$ (which corresponds to 4σ) is used as the detection condition[11,33]. However, we used a bin-by-bin analysis with 19 energy bands, where in each band the point source amplitude was not allowed to take on a negative value. As shown in Supplementary Section 2, we thus have a mixture distribution given by

$$p(\mathrm{TS}) = 2^{-n}\left(\delta(\mathrm{TS}) + \sum_{i=1}^{n}\binom{n}{i}\chi^2_{i+2}(\mathrm{TS})\right) \tag{2}$$

where δ is the Dirac delta function, $\binom{n}{i}$ is a binomial coefficient and χ^2_{i+2} is a χ^2 distribution with $i+2$ degrees of freedom. To work out the number of σ of a detection, we evaluate the equivalent p value for a one-new-parameter case[34]:

$$\text{Number of}\,\sigma \equiv \sqrt{\text{Inverse CDF}(\chi_1^2, \mathrm{CDF}[p(\mathrm{TS}), \widehat{\mathrm{TS}}])} \tag{3}$$

where CDF and InverseCDF are the cumulative distribution and inverse cumulative distribution, respectively. The first argument of each of these functions is the distribution function and the second is the value the CDF or InverseCDF is evaluated at. The observed TS value is denoted by $\widehat{\mathrm{TS}}$. It follows that we use a threshold of $\mathrm{TS} \geq 41.8$ to correspond to a 4σ detection.

The total set of new point source candidates found in this work are displayed in Supplementary Fig. 1 along with the TS residual map obtained in our last iteration. Although the model including all the new point sources is a much better representation of the region of interest, a few hotspots still remain. These are, however, found to be below the detection threshold of $\mathrm{TS} \geq 41.8$ in the maximum-likelihood step. As can be seen from Supplementary Fig. 1, the X-bulge morphology is clearly visible in the residual TS values. Although along the Galactic plane, compared with Fig. 1 the X-bulge morphology is shifted to negative longitudes (a similar shift is seen in refs [3,8,35] with the use of different methods), this may be due to degeneracies between the X-bulge template and the amplitude of the 3FGL and new point sources around $l = 0$, $b = 0$. A similar phenomenon can be seen in figures 1 and 2 in ref. [36]. The Poisson noise is also very large in this region and so the mismatch did not have much bearing on the fit.

To identify possible multi-wavelength counterparts to the gamma-ray sources, we searched in the seed locations within the 68% containment of the point spread function for one of our highest energy bands ~0.1°—around each source in the ATNF pulsar[37], globular cluster[38], supernova remnant (SNR)[39] and the Roma-BZCAT blazar[40] catalogues for potential gamma-ray emitters. We found spatial overlaps for 18 of our 64 point source candidates (Supplementary Table 1). Note that this does not preclude the possibility that the other 46 point source candidates are real sources since high extinction towards the GC makes it difficult to have complete multi-wavelength source catalogues.

Our new point sources are compared to the 2FIG[41] in Supplementary Fig. 6. As can be seen, there is a reasonable overlap considering that the two analyses used different diffuse galactic emission templates and that 2FIG was based on a wider energy range (0.3 to 500 GeV) and time interval (7.5 years). It is reassuring that the majority of new 2FIG sources that are not associated with one of our new point sources are on a hotspot of our TS map. The list of point sources found in this work is provided in Supplementary Table 1.

Including the 3FGL sources, we had a total of 116 point source candidates in our $|l| \leq 7.5°$, $|b| \leq 7.5°$ region of interest. This is compatible with the 127 point source candidates found in ref. [3] for a disk-like region of interest with radius 10°.

New templates. *X-bulge.* We followed a procedure based on the method described in ref. [19] applied to the WISE data. To use this template in fitting the Fermi-LAT data, all pixels values below zero were set to zero in each median filtered exponential subtracted map and our template was then constructed by taking the average of the two resultant maps. The resulting template is displayed by the white contours in Fig. 1.

Boxy bulge. We assumed the triaxial model for the Galactic bulge derived in ref. [42]. This was obtained by fitting to COBE/DIRBE near-infrared (1.25–4.9 μm) data. We adopted the best-fitting model in that reference, which is Model S. This consists of a sech^2 function on the bar radial spatial profile. The template used in our analysis is shown in Supplementary Fig. 7.

Nuclear bulge. We used a map constructed from a near-infrared stellar density measurement of the central region of our Galaxy ($|l| \geq 3°$ and $|b| \geq 1°$) and subtracted a best-fit Galactic disk component[23]. To remove artificial sharp boundaries in the map induced by survey patches, all pixels below 15 stars arcmin^{-2} were set to zero. The resulting template is displayed by the black contours in Fig. 1.

Dark matter. We modelled the potential annihilating dark-matter signal in the GC as the square of an NFW density profile with an inner slope of 1.2, which had been shown to describe the GCE well in previous works[43–45]. The square of an NFW density profile is representative of a tentative annihilating dark-matter signal in the GC.

Fermi bubbles. As found by Acero et al.[8], we used two catenary curves of the form $10.5° \times (\cosh((l-1°)/10.5°)-1°)$ and $8.7° \times (\cosh((l+1.7°)/8.7°)-1°)$ for the Northern and the Southern bubbles, respectively.

Testing extended emission templates. We fitted the gamma-ray emission with our bin-by-bin method to derive fluxes that are independent of the choice of spectral model. Within each bin, the spectrum of the included point and extended sources were modelled as power laws with fixed spectral index of two. Owing to the small size of the bins, our results were not sensitive to the precise spectral index used. In each energy bin, the amplitudes of all included point sources and all included extended templates were simultaneously fitted. This allowed us to effectively marginalize over the statistical uncertainties. Table 1 shows the steps we took to evaluate whether a template was significantly detected. We started with the baseline model and then evaluated the TS of each new template. We then added the template with the highest TS to our model and repeated the procedure with this appended to the base model. We iterated through these steps until the highest TS value of a new template was below our 4σ threshold. For each new template, there are $n \times 19$ new parameters, where n is an integer. The probability distribution is the same as equation (2), except that the 19 should be replaced by $n \times 19$ and the χ^2_{i+2} should be replaced with χ^2_i as we are not fitting the positions of the template. This is the same formula as in case 9 in ref. [46]. For one new template being considered (that is, 19 new parameters), our 4σ detection threshold corresponded to $\text{TS} \geq 38.4$.

The contributions of the different components for our proposed model of the GCE are shown in Supplementary Fig. 8. The fractional residuals are shown in Supplementary Fig. 9. As can be seen from the top left panel, the X-bulge is needed even when the interpolated gas maps are used. Comparing the top and bottom right panels shows that the X-bulge morphology has been accounted for by our template.

Molecular-hydrogen-to-CO conversion factor. Our inferred molecular-hydrogen-to-CO conversion factor (X_{CO}) is shown in Supplementary Table 2. As in ref. [8], we evaluated X_{CO} using our 2 GeV energy bin fit results. Our values are consistent with the results from all sky fits as can be seen by comparing to Fig. 25 in ref. [47]. Although our 8 to 10 kpc best-fit X_{CO} is larger than those obtained to fits of all of the sky and high-latitude[48] measurements, it does have large error bars and thus is still consistent with the other measurements at about the 2σ or better level even when only statistical errors are accounted for. As in ref. [47], our X_{CO} values for the outer annuli were strongly biased because the model under-fitted the data in the outer galaxy and thus we have not reported them.

We found that most of our results were not sensitive to changing the number of annuli to five. This was done by splitting our first annuli into two annuli with radii 0 to 1.5 kpc and 1.5 to 3.5 kpc as in ref. [3]. However, we achieved unrealistic X_{CO} values for the innermost annuli in that case. Therefore, we stuck to the four-annuli case shown in Supplementary Fig. 2. Note that we did not explicitly use the X_{CO} values in performing our fits and we are only quoting their inferred values to demonstrate that the fitted amplitudes for our interstellar gas maps are reasonably consistent with previous results.

Systematic errors. Our analysis involved making choices for the spin temperature, the cosmic-ray source distribution, the interstellar (denoted $E(B-V)$) reddening map magnitude cut, and also whether or not to include a template for the Fermi bubbles. We evaluated the associated systematic errors by seeing how the best-fit exponential cut-off parameters changed when different choices were made. To do this for the spin temperature, we used $T_S = 150$ K instead of $T_S = 170$ K. For the inverse Compton model, we changed the cosmic ray source distribution from Lorimer to OBstars[47] as this was found to have the greatest effect on the inverse Compton morphology. We found that changing other parameters for the inverse Compton model had negligible effects. The dust systematic error was evaluated by changing the $E(B-V)$ reddening map magnitude cut from 5 mag and above to 2 mag and above. The Fermi bubbles systematic error was obtained by including the catenary template in the fit. The resulting systematic errors are given in Table 2.

We also checked the sensitivity of our results to the background model and new point sources. As can be seen from Supplementary Table 3, the Xbulge+nuclear bulge are still needed when no new point sources are included, or when the interpolated gas maps are used, or when the 2FIG point sources are used. The NFW-squared template was still needed, after the X-bulge and nuclear bulge were included, only in the case of the interpolated gas maps.

To evaluate the impact that potential mismodelling of the Galactic plane could have in our main results we masked the inner $|b| < 1°$ of the region of interest (Supplementary Fig. 10) and utilized a statistical procedure similar to that in Table 1. We used the Composite2 tool within the Fermi Science Tools and performed a composite likelihood analysis of the unmasked region of interests simultaneously for each energy bin (this method was first used in the GC region in ref. [15]). We combined the regions $b > 1°$ and $b < -1°$ of the inner $15° \times 15°$ of the GC and constrained the normalization of all the extended templates to be the same throughout the two separate region of interests at each energy bin. The majority of the new point sources as well as the nuclear bulge template reside in the $|b| < 1°$ region, so this analysis pipeline considered the 22 new point sources outside the masked region, the X-bulge and the NFW-squared templates in an attempt to model the GCE. The results are shown in Supplementary Table 4. As can be seen, the data still significantly favour an X-bulge template over a spherical template.

As an additional check, we also evaluated the correlation matrix around our best-fit model. We found that the correlation coefficients between all extended components and our X-bulge and nuclear bulge templates were in the range 10^{-10} to 10^{-2} in all energy bins. With such small correlations, even systematic biases in the templates several times larger than the statistical uncertainties would not substantially affect the fitted normalizations of the two bulge templates. Further sources of systematic errors may arise from the choices made in constructing the X-bulge and nuclear bulge templates. We will investigate these in future work.

Data availability. Data that support the plots within this paper and other findings of this study are available from the corresponding author upon reasonble request.

Received: 28 April 2017; Accepted: 6 February 2018;
[redacted]

References

1. Atwood, W. B. et al. The Large Area Telescope on the Fermi Gamma-Ray Space Telescope mission. *Astrophys. J.* **697**, 1071–1102 (2009).
2. Goodenough, L. & Hooper, D. Possible evidence for dark matter annihilation in the inner Milky Way from the Fermi Gamma Ray Space Telescope. Preprint at http://arxiv.org/abs/0910.2998 (2009).
3. Ackermann, M. et al. The Fermi Galactic Center GeV excess and implications for dark matter. *Astrophys. J.* **840**, 43 (2017).
4. Calore, F., Cholis, I. & Weniger, C. Background model systematics for the Fermi GeV excess. *J. Cosm. Astropart. Phys.* **3**, 38 (2015).
5. Abazajian, K. N. & Kaplinghat, M. Detection of a gamma-ray source in the Galactic Center consistent with extended emission from dark matter annihilation and concentrated astrophysical emission. *Phys. Rev.* **D 86**, 083511 (2012).
6. O'Leary, R. M., Kistler, M. D., Kerr, M. & Dexter, J. Young pulsars and the Galactic Center GeV gamma-ray excess. Preprint at http://arXiv.org/abs/1504.02477 (2015).

7. Cholis, I. et al. The Galactic Center GeV excess from a series of leptonic cosmic-ray outbursts. *J. Cosm. Astropart. Phys.* **12**, 005 (2015).
8. Acero, F. et al. Development of the model of Galactic interstellar emission for standard point-source analysis of Fermi Large Area Telescope data. *Astrophys. J. Suppl.* **223**, 26 (2016).
9. Macias, O. & Gordon, C. Contribution of cosmic rays interacting with molecular clouds to the Galactic Center gamma-ray excess. *Phys. Rev.* **D 89**, 063515 (2014).
10. Pohl, M., Englmaier, P. & Bissantz, N. Three-dimensional distribution of molecular gas in the barred Milky Way. *Astrophys. J.* **677**, 283–291 (2008).
11. Acero, F. et al. Fermi Large Area Telescope third source catalog. *Astrophys. J. Suppl.* **218**, 23 (2015).
12. Keeley, R., Abazajian, K., Kwa, A., Rodd, N. & Safdi, B. What the Milky Way's dwarfs tell us about the Galactic Center extended excess Preprint at http://arXiv.org/abs/1710.03215 (2017).
13. Lee, S. K., Lisanti, M., Safdi, B. R., Slatyer, T. R. & Xue, W. Evidence for unresolved γ -ray point sources in the inner galaxy. *Phys. Rev. Lett.* **116**, 051103 (2016).
14. Bartels, R., Krishnamurthy, S. & Weniger, C. Strong support for the millisecond pulsar origin of the Galactic Center GeV excess. *Phys. Rev. Lett.* **116**, 051102 (2016).
15. Horiuchi, S., Kaplinghat, M. & Kwa, A. Investigating the uniformity of the excess gamma rays towards the Galactic Center region. *J. Cosm. Astropart. Phys.* **1611**, 053 (2016).
16. Ploeg, H., Gordon, C., Crocker, R. & Macias, O. Consistency between the luminosity function of resolved millisecond pulsars and the Galactic Center excess. *J. Cosm. Astropart. Phys.* **1708**, 015 (2017).
17. Portail, M., Wegg, C. & Gerhard, O. Peanuts, brezels and bananas: food for thought on the orbital structure of the Galactic bulge. *Mon. Not. R. Astron. Soc.* **450**, L66–L70 (2015).
18. Nataf, D. M., Udalski, A., Gould, A., Fouqué, P. & Stanek, K. Z. The split red clump of the Galactic Bulge from OGLE-III. *Astrophys. J. Lett.* **721**, L28–L32 (2010).
19. Ness, M. & Lang, D. The X-shaped bulge of the Milky Way revealed by WISE. *Astrophys. J.* **152**, 14 (2016).
20. Wright, E. L. et al. The Wide-field Infrared Survey Explorer (WISE): mission description and initial on-orbit performance. *Astrophys. J.* **140**, 1868–1881 (2010).
21. Joo, S.-J., Lee, Y.-W. & Chung, C. New insight on the origin of the double red clump in the Milky Way bulge. *Astrophys. J.* **840**, 98 (2017).
22. Launhardt, R., Zylka, R. & Mezger, P. G. The nuclear bulge of the Galaxy. III. Large-scale physical characteristics of stars and interstellar matter. *Astron. Astrophys.* **384**, 112–139 (2002).
23. Nishiyama, S. et al. Magnetically confined interstellar hot plasma in the nuclear bulge of our Galaxy. *Astrophys. J. Lett.* **769**, L28 (2013).
24. Ackermann, M. et al. The spectrum and morphology of the Fermi bubbles. *Astrophys. J.* **793**, 64 (2014).
25. Su, M., Slatyer, T. R. & Finkbeiner, D. P. Giant gamma-ray bubbles from Fermi-LAT: active galactic nucleus activity or bipolar galactic wind? *Astrophys. J.* **724**, 1044–1082 (2010).
26. Bland-Hawthorn, J. & Gerhard, O. The Galaxy in context: structural, kinematic, and integrated properties. *Annu. Rev. Astron. Astrophys.* **54**, 529–596 (2016).
27. Winter, M., Zaharijas, G., Bechtol, K. & Vandenbroucke, J. Estimating the GeV emission of millisecond pulsars in dwarf spheroidal galaxies. *Astrophys. J.* **832**, L6 (2016).
28. Abdo, A. A. et al. A population of gamma-ray emitting globular clusters seen with the Fermi Large Area Telescope. *Astron. Astrophys.* **524**, A75 (2010).
29. Bartels, R., Storm, E., Weniger, C. & Calore, F. The Fermi-LAT GeV excess traces stellar mass in the Galactic bulge. Preprint at http://arXiv.org/abs/1711.04778 (2017).
30. Strong, A. W. et al. Galprop version 54: explanatory supplement. https://galprop.stanford.edu/download/manuals/galprop_v54.pdf (2011).
31. Ajello, M. et al. Fermi-LAT observations of high-energy γ-ray emission toward the Galactic center. *Astrophys. J.* **819**, 44 (2016).
32. Nolan, P. L. et al. Fermi Large Area Telescope second source catalog. *Astrophys. J. Suppl.* **199**, 31 (2012).
33. Mattox, J. et al. The likelihood analysis of EGRET data. *Astrophys. J.* **461**, 396 (1996).
34. Wilks, S. S. The large-sample distribution of the likelihood ratio for testing composite hypotheses. *Ann. Math. Stat.* **9**, 60 (1938).
35. Yang, R.-Z. & Aharonian, F. On the GeV excess in the diffuse γ-ray emission towards the Galactic centre. *Astron. Astrophys.* **589**, A117 (2016).
36. Gordon, C. & Macias, O. Dark matter and pulsar model constraints from Galactic center Fermi-LAT gamma ray observations. *Phys. Rev.* **D 88**, 083521 (2013).
37. Manchester, R. N., Hobbs, G. B., Teoh, A. & Hobbs, M. The Australia Telescope National Facility pulsar catalogue. *Astron. J.* **129**, 1993–2006 (2005).
38. Harris, W. E. A catalog of parameters for globular clusters in the Milky Way. *Astron. J.* **112**, 1487 (1996).
39. Green, D. A. A catalogue of 294 Galactic supernova remnants. *Bull. Astron. Soc. India* **42**, 47–58 (2014).
40. Massaro, E. et al. Roma-BZCAT: a multifrequency catalogue of blazars. *Astron. Astrophys.* **495**, 691–696 (2009).
41. Fermi-LAT Collaboration Characterizing the population of pulsars in the Galactic bulge with the Fermi Large Area Telescope. Preprint at https://arxiv.org/abs/1705.00009 (2017).
42. Freudenreich, H. T. A COBE model of the Galactic bar and disk. *Astrophys. J.* **492**, 495–510 (1998).
43. Hooper, D. & Linden, T. On the origin of the gamma rays from the Galactic center. *Phys. Rev.* **D 84**, 123005 (2011).
44. Abazajian, K. N., Canac, N., Horiuchi, S. & Kaplinghat, M. Astrophysical and dark matter interpretations of extended gamma-ray emission from the Galactic center. *Phys. Rev.* **D 90**, 023526 (2014).
45. Daylan, T. et al. The characterization of the gamma-ray signal from the central Milky Way: a case for annihilating dark matter. *Phys. Dark Univ.* **12**, 1–23 (2016).
46. Self, S. G. & Liang, K.-Y. Asymptotic properties of maximum likelihood estimators and likelihood ratio tests under nonstandard conditions. *J. Am. Stat. Assoc.* **82**, 605–610 (1987).
47. Ackermann, M. et al. Fermi-LAT observations of the diffuse gamma-ray emission: implications for cosmic rays and the interstellar medium. *Astrophys. J.* **750**, 3 (2012).
48. Casandjian, J.-M. Local Hi emissivity measured with Fermi-LAT and implications for cosmic-ray spectra. *Astrophys. J.* **806**, 240 (2015).

Acknowledgements

R.M.C. was the recipient of an Australian Research Council Future Fellowship (FT110100108). S.H. is supported by the U.S. Department of Energy, Office of Science, under award number de-sc0018327. We thank D. Lang for making available code and data that helped with generating the X-bulge template and both S. Nishiyama and K. Yasui for providing the data for the nuclear bulge template. We acknowledge the use of public data and software from the Fermi data archives (http://fermi.gsfc.nasa.gov/ssc/). Finally, the authors would also like to thank F. Aharonian, A. M. Brown, F. Calore, J.-M. Casandjian, H. T. Cromartie, S. Digel, T. Enßlin, M. Kaplinghat, K. Freeman, O. Gerhard, O. Gnedin, X. Huang, N. McClure-Griffiths, D. Nataf, H. Ploeg, B. Roberts, M. Winter, R. Tuffs and G. Zaharijas for enlightening discussions.

Author contributions

O.M. designed and performed the majority of the data analysis. O.M. also constructed the Fermi bubbles, Sun, Moon, inverse Compton and Loop I templates. C.G. processed the WISE data and derived the mixture distribution formulas. R.M.C. suggested the link with the X-bulge. B.C. processed the hydrodynamical 3D map into annuli density maps. D.P. created the interpolated annuli density maps. C.G. and S.H. assisted with the point source modelling. B.C. and D.P. created the dust maps. M.P. created the 3D HI and CO maps. All authors contributed to the interpretation of the results. The text of the final manuscript was mainly written by O.M. and C.G., but all authors had some contribution.

Competing interests

The authors declare no competing interests.

Additional information

Supplementary information is available for this paper at https://doi.org/10.1038/s41550-018-0414-3.

Reprints and permissions information is available at www.nature.com/reprints.

Correspondence and requests for materials should be addressed to O.M.